Materials Science & Engineering A 654 (2016) 131–142

Contents lists available at ScienceDirect

Materials Science & Engineering A

journal homepage: www.elsevier.com/locate/msea

Grain refinement kinetics and strengthening mechanisms in Cu–0.3Cr–0.5Zr alloy subjected to intense plastic deformation

A.P. Zhilyaev [a,*], I. Shakhova [b], A. Morozova [b], A. Belyakov [b], R. Kaibyshev [b]

[a] Institute for Metals Superplasticity Problems, Khalturina 39, Ufa 450001, Russia
[b] Belgorod State University, Pobeda 85, Belgorod 308015, Russia

ARTICLE INFO

Article history:
Received 15 October 2015
Received in revised form
10 December 2015
Accepted 12 December 2015
Available online 15 December 2015

Keywords:
CuCrZr alloy
Grain refinement
Solid solution
Aging
Intense plastic deformation

ABSTRACT

The ultrafine-grained microstructures, mechanical properties and electrical conductivity of a Cu–0.3%Cr–0.5%Zr alloy subjected to equal channel angular pressing (ECAP) at a temperature of 400 °C to a total strain of 1, 2, and 4 were investigated. The ultrafine-grained microstructure resulting from progressive increase in the misorientations of strain-induced low-angle boundaries during the multiple ECAP process is considered as a type of continuous dynamic recrystallization. The multiple ECAP process resulted in substantial strengthening of the alloy. The yield stress of CuCrZr alloy in the initial solution treated condition (ST) increased from 65 MPa to 476 MPa after four ECAP passes at 400 °C. For the aged condition (AT), the yield stress increased from 170 MPa to 511 MPa after four passes. The strengthening was attributed to the grain refinement and high dislocation densities evolved via large strain deformation. Bacon–Kocks–Scattergood modification of the Orowan model is sufficient for acceptable description of the precipitation hardening of AT specimens during ECAP processing; this finding is in excellent agreement with the experimental data. The discrepancy between the experiment and model for ST specimens disappears after taking into consideration additional precipitating of the supersaturated solid solution during preheating and ECAP processing.

1. Introduction

Age-hardenable Cu–Cr–Zr alloys are widely used in numerous applications due to the excellent combination of moderate strength with high electrical or thermal conductivity [1–6]. These alloys are advanced materials for railway contact wire, resistance welding electrodes, electronic commutators and the heat sink of the International Thermonuclear Experimental Reactor (ITER) diverter [1–3]. There is a demand for a high speed train on electric railways to improve the strength and conductivity performance of contact wires [4–6]. The target for the new material of contact wires is an alloy with an ultimate tensile strength (UTS) higher than 530 MPa and electrical conductivity over 78 pct IACS (International Annealed Copper Standard). However, strength and electrical/thermal conductivity have opposing characteristics. Copper and its alloys may be strong or conductive but are rarely both. The alloying of one or more metals or non-metals is a well-established approach for improving the mechanical properties, such as yield stress (YS), UTS and hardness. In addition to the alloying, the tensile response of materials can be optimized via aging or quenching, which result in changes to the microstructure. The high strength of Cu–Cr–Zr alloys is attributed to precipitation of nanoscale dispersoids, and the high electrical/thermal conductivity is due to the low solubility of Cr and Zr in Cu [4–11]. From this alloying philosophy, the Cu–Cr–Zr alloys are subjected to certain processes, such as aging treatment (AT) and solution treatment (ST), for the formation of the optimal distribution of secondary phase particles and a pure Cu matrix with a negligible amount of solutes, which strongly reduce the electrical/thermal conductivity.

Recently, a promising approach to strengthening Cu–Cr–Zr alloys while retaining their electric conductivity at a sufficiently high level (80% IACS) was developed [7–11]. This approach involves a large strain deformation followed by a final aging that enables the formation of an ultrafine-grained structure stabilized by nanoscale precipitations. At room temperature the contributions of dispersoids and grain boundaries to the reduction of electrical conductivity are negligible comparing electron scattering by phonons. At the same time, dispersoids and grain boundaries provide an UTS of approximately 600 MPa or higher through dispersion hardening and grain size strengthening [2,6,10,11]. Currently, this combination of strength and conductivity that provided by the superposition of ultrafine-grained (UFG) structure, nanoscale coherent dispersoids and low-solute-content copper

* Corresponding author.
E-mail address: AlexZ@anrb.ru (A.P. Zhilyaev).

http://dx.doi.org/10.1016/j.msea.2015.12.038
0921-5093/

containing only traces of Cr and Zr is one of the best for copper and copper alloys.

The precipitation sequence, the size and distribution for coherent Cr-rich phase particles have been considered in Cu–Cr alloys [6,12–15]. The distribution of secondary phase particles in the Cu–Cr–Zr alloys has been considered in several works and clearly summarized in recent reports [10,11].

Grain refinement via intense plastic deformation provides structural strengthening consistent with the Hall–Petch relationship [16]. Recently, many techniques of intense plastic working such as multidirectional forging [17], equal channel angular pressing [18–20], high pressure torsion [21–23] and accumulative roll-bonding [24] were applied to produce the UFG structure in metallic materials including Cu–Cr–Zr alloys. The structural evolution leading to the formation of ultrafine grains in the Cu–0.3% Cr–0.5%Zr alloy during multidirectional forging up to a total strain of 4 at 20 and 400 °C was recently studied for both ST and AT samples [10]. The deformation behavior was characterized by a rapid increase in the flow stress at an early deformation, followed by a steady-state flow at large strain. The development of the new ultrafine grains resulted from the progressive increase in the misorientations of the strain-induced low-angle boundaries, which evolve into high-angle boundaries (HAB) with increasing cumulative strain through a strain-induced continuous reaction that is quite similar to continuous dynamic recrystallization (cDRX). The formation of ultrafine grains was closely related to the development of geometrically necessary boundaries, which is attributed to deformation banding. The grain refinement kinetics increased as the deformation temperature increased. Similar results were obtained for the Cu–0.87%Cr–0.06%Zr alloy subjected to ECAP at temperatures of 200–400 °C [11]. The new ultrafine grains resulted from progressive increase in the misorientations of strain-induced low-angle boundaries during the multiple ECAP process. The development of ultrafine-grained microstructures is considered as a type of cDRX. The multiple ECAP process resulted in substantial strengthening of the alloy. The YS increased from 215 MPa in the original peak aged condition to 480 MPa and 535 MPa after eight ECAP passes at 400 °C and 200 °C, respectively. The strengthening was attributed to the grain refinement and high dislocation densities evolved during large strain deformation. Modified Hall–Petch analysis indicated that the contribution of dislocation strengthening to the overall increment of YS through ECAP was higher than that of grain size strengthening. The formation of ultrafine grains containing high dislocation density led to a small reduction in electrical conductivity from 80% to 70% IACS.

One of the previous report [10] has dealt with the alloys under our consideration (Cu–0.3Cr–0.5Zr) but used multidirectional forging, while the other [11] employed the method of intense plastic deformation used in the current work (ECAP) but applied it to a "classical" alloy (Cu–1Cr–0.1Zr). Applying ECAP for grain refinement, we have a unique option to compare results obtained in the current work with reports [10,11]. Therefore, the aim of the present report is to evaluate the effectiveness of grain refinement of the Cu–0.3Cr–0.5Zr alloy subjected to (i) solution treatment (ST) and (ii) consequent aging treatment (AT) prior to intense plastic deformation by means of equal channel angular pressing. The effectiveness is evaluated with respect to structural characteristics: (i) kinetics of dislocation accumulation; (ii) grain refinement; (iii) kinetics of HAB accumulation; (iv) microtexture evolution. The role of different strengthening mechanisms, including: (i) Peierls–Nabarro stress; (ii) dislocation strengthening; (iii) Hall–Petch hardening; (iv) solid solution strengthening; (v) precipitation hardening, will be analyzed, and functional properties (electroconductivity) vs. strength and ductility in ST and AT alloys will be reviewed. We also apply three methods of characterization (X-ray, transmission electron microscopy and electron backscatter diffraction) to the same alloy and obtain and compare all microstructural parameters (e.g., grain size and dislocation density). These parameters are introduced to the known model of strengthening mechanisms to verify their applicability in practice.

2. Experimental

An alloy of Cu–0.3Cr–0.5Zr (wt%) was subjected to two-step heat treatment. The first step involved solution treatment at a temperature of 920 °C for 30 min followed by water quenching. These samples are designated as solution treated (ST) samples in the text. The second step was to age the ST samples at 450 °C for 1 h. They are henceforth denoted as aging treated (AT) samples. Bilets in both conditions were subjected to equal channel angular pressing (ECAP) under the isothermal condition at 400 °C to total strains of approximately 1, 2, and 4. Some of the ST billets were processed to a total strain of 8. Selected experimental data were analyzed for them. The billets with a starting dimension of $14 \times 14 \times 90\ mm^3$ were preheated for 30 min at 400 °C and then pressed through a die with an angle of 90° via route Bc (90° anticlockwise rotation of the specimens after each pass). The processed samples were cooled in water after reaching the required total strain.

The microstructural investigations were performed using a Quanta 600 FEG scanning electron microscope (SEM) equipped with an electron backscattering diffraction (EBSD) analyzer incorporating an orientation-imaging microscopy (OIM) and Jeol JEM-2100 transmission electron microscope (TEM). The specimens for microstructure investigation were cut from the central part of deformed samples in the longitudinal direction parallel to the last pressing direction, i.e., the deformation microstructures in the longitudinal plane *Y* from the central part of the deformed samples were investigated. The specimens for SEM investigation were mechanically polished to a mirror-like state using a 1000-grit SiC paper, followed by a final polishing on a diamond suspension with a particle size of 3 μm. The next step of specimen preparation consisted of electrochemical polishing at room temperature using an electrolyte of HNO_3:CH_3OH=1:3 with a voltage of 10 V. The EBSD scans were performed with a step of 100 nm for the samples strained to ~1 and 50 nm for samples strained to ~2 and 4, and then the EBSD maps were subjected to a clean-up procedure, setting a minimal confidence index of 0.1. Thin foils for TEM investigation were electro-polished using the aforementioned electrolyte at a temperature of −15 °C using a Tenupol 5 twinjet polishing unit. An average grain size *D* was estimated by using the linear intercept method on the TEM micrographs, counting all the clearly visible boundaries/sub-boundaries. The dislocation density was measured by counting the individual dislocations in the grain/sub-grain interiors in at least 5 arbitrarily selected TEM images for each data point. The X-ray diffraction (XRD) measurements were performed using ARL X'TRA machine. The crystallite size (or coherent domain size, *d*) and microstrain ($\langle \varepsilon^2 \rangle^{1/2}$) were estimated based on the Rietveld method [25] using MAUD software [26] to accomplish the profile fitting of the experimental XRD scan. The electrical conductivities of the investigated samples were measured using the four-point probe method [27]. The specimens for the conductivities were mechanically polished to a mirror-like state as described above. The tensile tests were carried out using an Instron 5882 testing machine on specimens with a gauge length of 16 mm and cross-section of 1.5 mm × 3 mm oriented with the tensile direction parallel to the ECAP sample axes at a strain rate of $2 \cdot 10^{-3}\ s^{-1}$ at room temperature.

3. Results

3.1. Initial microstructure

The alloy initially had an average grain size of ~700 μm (Fig. 1a) and a low dislocation density of $\rho \sim 3 \cdot 10^{12}$ m^{-2}. At 920 °C, Zr and Cr did not dissolve completely, and some particles with an average size of ~180 nm were present in the ST specimen as indicated by arrows in Fig. 1b. The particles composition and stoichiometry were determined in the previous report [10]. The aging led to precipitating chromium-rich particles that had round shapes and sizes less than 10 nm. These particles exhibited the Nishiyama–Wassermann orientation relationship with the copper matrix. The typical structure of the AT state is represented in Fig. 1c.

To estimate the precipitation strengthening effect on refinement kinetics in the AT specimens during consequent ECAP, the size of Cr particles (D_P) and their volume fraction (F_V) were estimated in selected areas of the TEM micrograph shown in Fig. 1c. The mean diameter of Cu-rich precipitates, D_P, measured was 2.5 ± 0.1 nm; volume fraction, $F_V = 0.015\%$. For randomly distributed particles, the center-to-center nearest neighbor spacing on a plane (L_P) was calculated as [28]:

$$L_P = \frac{D_P}{2}\sqrt{\frac{\pi}{6F_V}} = 73.9\,\text{nm}. \tag{1}$$

The correctness of the estimation of volume fraction can be verified using the results of atomic probe tomography (APT) on the Cu–1Cr–0.1Zr alloy published by Chibihi et al. [12]. They measured the Cr concentration in the fcc copper matrix as a function of annealing time. The plot of the first column of Table 1 [12] is shown in Fig. 2. As expected, there was an exponential dependence on annealing time:

$$C_{Cr}(t_{ANN}) = A \cdot e^{-0.36 \cdot t} \tag{2}$$

A pre-exponential coefficient, A, is the initial concentration of chromium atoms in the Cu matrix. The aging temperature in our experiments $T = 450$ °C was close to the temperature of 440 °C used in [12]. Assuming similar decomposition kinetics for the Cu–0.3Cr–0.5Zr alloy, we can estimate the retained concentration of Cr in the matrix for an aging time of 1 h as $0.3 \cdot e^{-0.36 \cdot 1} = 0.24\%$. The number of chromium atoms per one particle can be estimated as

$$n \cong \left(\frac{D_P/2}{a_{Cr}}\right)^3 = 700, \tag{3}$$

where $a_{Cr} = 140$ pm is the average atomic radius of chromium. The volume fraction of chromium atoms located in Cr-precipitates equals 0.05%, and retained chromium of 0.25% is dissolved in the copper matrix. Two independent estimations gave volume fractions close to that of the chromium, supporting the correctness of estimated values for a volume fraction (F_V), average diameter (D_P) and particles spacing (L_P) of Cr precipitates. Supposing that during ECAP there are no significant changes in the size and volume fraction of Cr-precipitates, one can estimate strengthening due to the particles using the Bacon–Kocks–Scattergood (BKS) model [29]:

$$\sigma_{BKS} = A\frac{MGb}{L}\left[ln\left(\frac{\bar{D}}{2b}\right) + 0.7\right], \tag{4}$$

where A is a coefficient related to the type of dislocations (edge or screw) and equals approximately 0.2, $L = L_P - D_P$ is the spacing between particles, M is the Taylor factor, $G = 42.1$ GPa is the shear modulus of copper, and b is Burgers vector of the copper matrix [30]. In BKS model

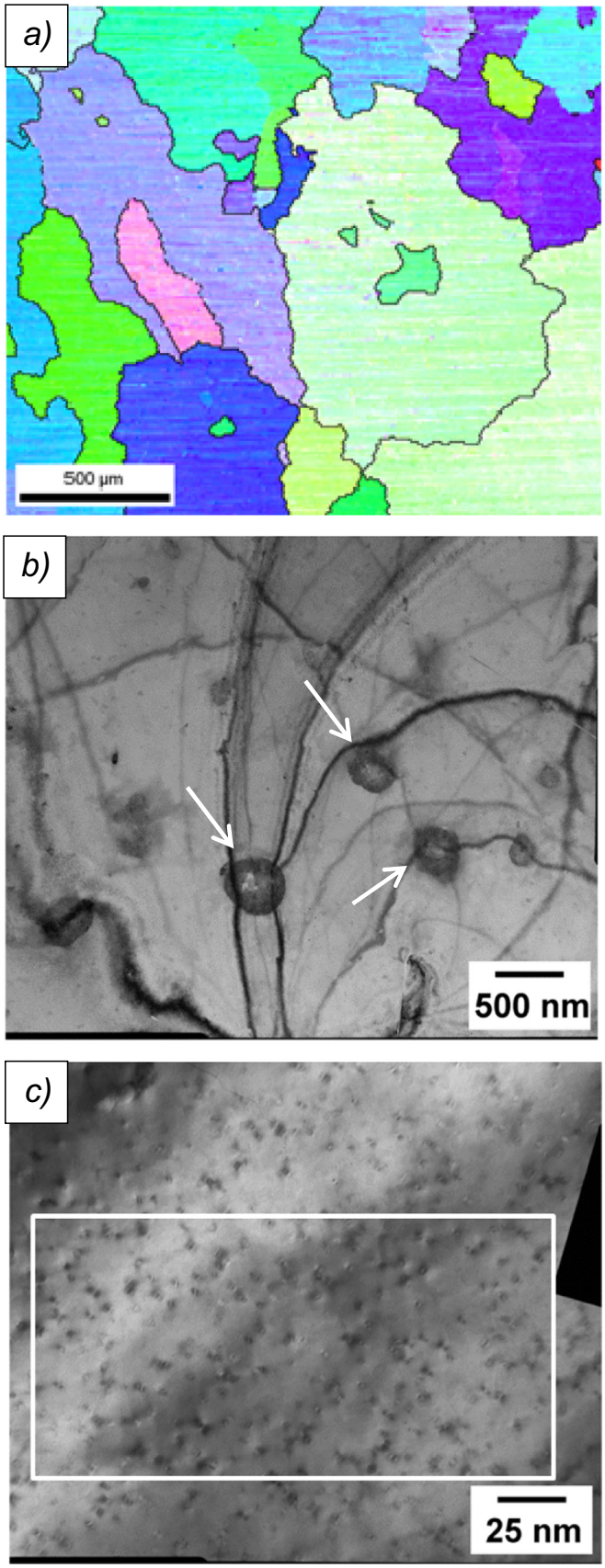

Fig. 1. (a) EBSD map of the initial microstructure; (b) is TEM micrograph of Cu–Cr–Zr alloy after solution treatment and (c) is TEM micrograph of AT condition (a region outlined by white lines was used for the analysis of precipitate size and distribution).

Table 1
(Sub-)grain size, *d* (nm) evaluated by TEM, EBSD and X-ray.

Number of ECAP passes	TEM		EBSD		X-ray	
	ST	AT	ST	AT	ST	AT
0	61,800	116,300	88,800	88,800	640.9	640.9
1	407.4	302.2	420	570	252.6	279.2
2	267.6	230.1	340	350	227.2	243.9
4	216.2	203.7	330	340	198.3	208.9

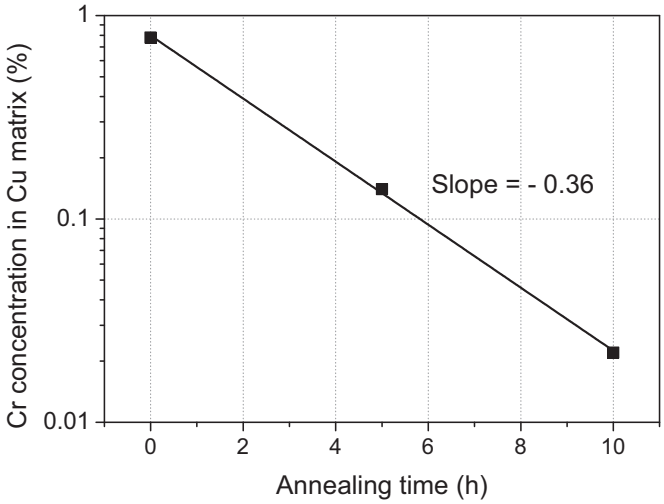

Fig. 2. Cr concentration in copper matrix as a function of annealing time plotted using data of the Table 1 of the report [12].

$$\bar{D} = \frac{D_P \cdot L}{D_P + L} = 2.42\,\text{nm} \tag{5}$$

is a harmonic average that describes the two limit cases of the Orowan strengthening problem. When L_P, i.e., the spacing between precipitates, is low compared to D_P, the dislocation bows out between precipitates without a strong "dipolar" interaction between sections of dislocations on the opposite side of the precipitates; thus, $\bar{D} \cong L$. Alternatively, when the precipitate diameter D_P is small compared to L_P, the "dipolar" interactions become large and $\bar{D} \cong D_P$. It can be assumed that in Eq. (4), only the Taylor factor can change during severe plastic deformation. The order of precipitation strengthening then can be estimated for $M=3$: $\sigma_{BKS} \sim 147$ MPa, which is a quite reasonable value for the Cu–Cr–Zr alloy in peak aged condition.

Similar estimation can be performed for the ST state, where the diameter of particles is approximately 180 nm and inter-particles distance is approximately 1400 nm (Fig. 1b). Eq. (4) gives approximately 26.5 MPa for precipitation strengthening, which is comparable with the Peierls-Nabarro hardening (25 MPa) for a copper matrix.

3.2. Deformation microstructure

3.2.1. TEM study

Fig. 3 depicts an evolution of grain structure of the Cu–Cr–Zr alloy in two conditions (solution treated and aged) during ECAP processing to strains of ~1, 2 and 4 corresponding to 1, 2 and 4 passes along the route Bc. The numbers near GBs indicate a misorientation angle of two neighbor grains. It is apparent from Fig. 3 that grain refinement occurs more intensively in the ST condition compared to the AT one for the first ECAP pass. However, most GBs in the ST condition are low-angle boundaries. In the AT condition, a large primary grain has remained undistorted, being in a not easy-slipping orientation. After 2 passes, both microstructures are quite similar, with a high fraction of GBs with misorientations larger than 10°. A similar conclusion can be made by comparing the microstructure of the Cu–Cr–Zr alloy in both (ST and AT) conditions after four passes. With increasing strain, the deformation bands become subdivided by the transverse low-angle boundaries, thereby increasing the misorientations of longitudinal boundaries. This behavior results in the formation of equiaxed crystallites bounded by low-to-high-angle boundaries (Fig. 3). The mean grain sizes, estimated by using several TEM micrographs using the intercept method for Cu–Cr–Zr alloys in both conditions (solution treated and aged) as a function of ECAP passes, are summarized in Table 1. No large precipitates were detected at this level of magnification, indicating that there is no significant change in size and distribution of the Cr-particles in the ST condition subjected to intense plastic deformation. It is believed that chromium-rich particles may be re-distributed by the shear, but their size and inter-particles distance remain substantially unchanged.

Table 2 gives the dislocation density in both conditions of the Cu-alloy as a function of accumulated strain estimated by TEM. Commonly, the deformation microstructures contain a very high dislocation density, although the levels of dislocation accumulation in ST and AT samples are not the same. There is a significant increase in dislocation density in the ST specimen after one ECAP pass. Moreover, the total accumulated dislocation density after four passes in the solution treated sample is noticeably higher than in the aged specimen after four passes of ECAP.

3.2.2. EBSD study

Fig. 4 represents inverse pole figure maps (left column), recrystallization maps (middle column) and (111) pole figures of the ST samples subjected to ECAP for one, two and four passes. From the IPF maps (left column), one can see that separate deformation bands appear in the ST specimen after one pass. The (111) pole figure in the right column corresponds to a quite strong (17.5x random) C-component of shear texture, with some other maxima of the main components spread out. Therefore, the portions of original grains rapidly rotate toward several stable orientations. Straining for 2 passes leads to substantial dividing of the microstructure into a band structure with a band width of approximately 1 μm or less. This correlates with the fine band structure shown in the left column, and the texture component (right column) coincides with two variants of B-fiber, which explains the intermediate strength of texture maxima. Apparently, further straining for 4 passes does not refine the microstructure, and deformation bands remain in the IPF map. The texture strength increases again (11.8x random) due to reorientation of lattice to several ideal orientations.

Structures of aged specimens during progressive ECAP straining evolve differently (Fig. 5). The wide band structure (~10 μm), which represents two variants of B-fiber texture (Fig. 5, right column) separated by an angle of more than 10° and showing the maximal strength of the texture (15.7x random), can be observed in the AT specimen after one ECAP pass (Fig. 5, left column). The second ECAP pass activates a strong localization of deformation in shear bands with a width of approximately 1 μm. Further ECAP refines the microstructure, providing the formation of several families of mutually intersecting deformation bands within one initial grain. A distinct band-like structure evolves. Therefore, the aging promotes the occurrence deformation banding along several non-coplanar planes and decreases the thickness of deformation bands as under multidirectional forging [10]. The mean crystallite sizes evaluated using EBSD are summarized in the middle part of Table 1. Because they are area averaged (for GBs > 5° in misorientation), the values of crystallite sizes are slightly higher than

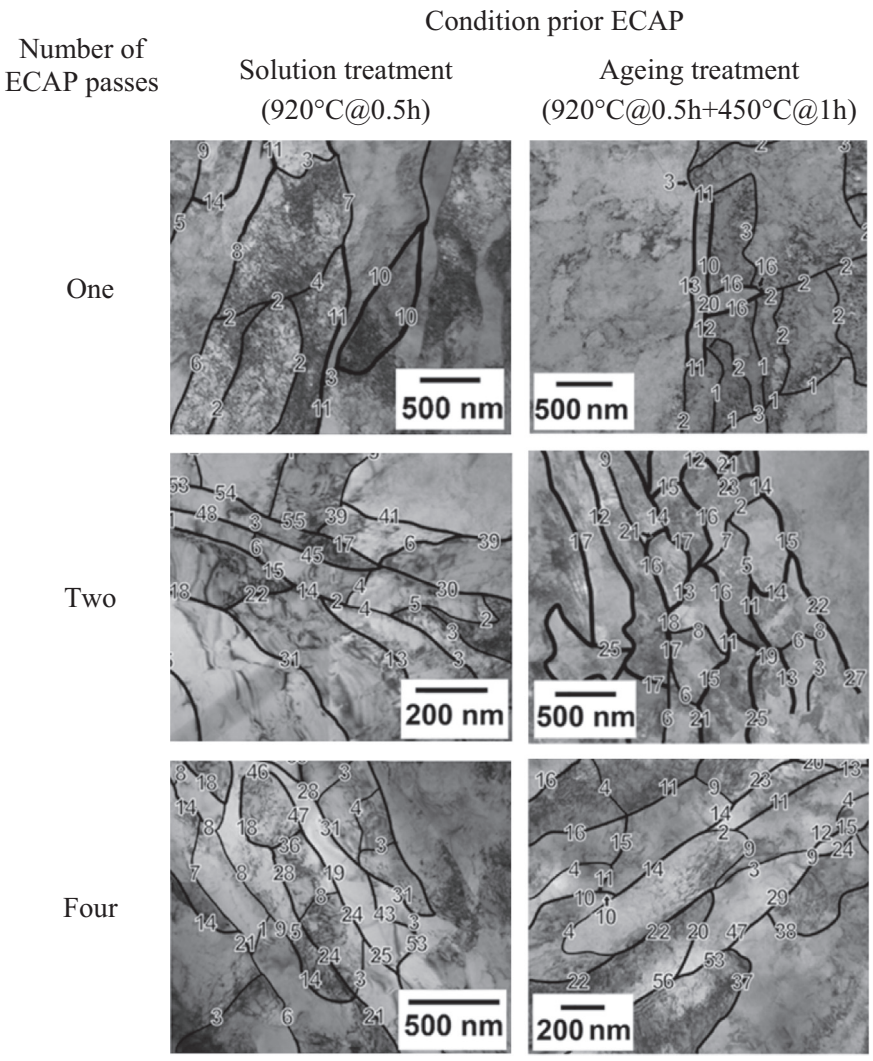

Fig. 3. TEM (bright field) micrographs of the fine structure CuCrZr alloy subjected to ECAP in ST (left column) and AT (right column) condition. The numbers near GBs indicate a misorientation angle of two neighbor grains.

Table 2
Dislocation density, $\rho \times 10^{14}$ (m^{-2}) evaluated by TEM, EBSD and X-ray.

Number of ECAP passes	TEM		EBSD		X-ray	
	ST	AT	ST	AT	ST	AT
0	1.6	2.4	0.1	0.1	0.2	0.2
1	6.0	5.6	8.3	7.3	0.9	0.3
2	6.9	6.3	13.0	13.4	0.6	0.4
4	9.2	7.3	14.0	12.6	0.7	0.5

those determined from TEM (left column of Table 1).

Using the Kernel average misorientation (KAM) option, one can evaluate the dislocation density via Frank's equation:

$$\theta \approx 2 \sin \frac{\theta}{2} = \frac{N \cdot b}{h}, \tag{6}$$

where θ is the misorientation created by a wall consisting of N dislocations of height h and b is the Burgers vector. In the EBSD experiments, the distance h corresponds to the step size of the scanning. Thus, the step size varies for unprocessed and processed specimens. The dislocation density ρ is then given by the ratio of the dislocation number to the surface area:

$$\rho = \frac{N}{S}, \tag{7}$$

where the surface area of the hexagon S as a function of a scanning step h is

$$S = \frac{\sqrt{3}}{2} h^2 \tag{8}$$

It follows that the dislocation density can be estimated from the relationship [31]:

$$\rho = \frac{2\sqrt{3}}{3} \cdot \frac{\theta}{b \cdot h} \tag{9}$$

The calculated dislocation density as a function of accumulated strain is given in Table 2 (middle part). Again, as for mean grain sizes, the values of dislocation density are higher than the ones measured from TEM.

3.2.3. X-ray analysis

All ECAP specimens in both conditions (ST and AT) have been analyzed with an X-ray to estimate the coherent domain size of crystallites and microstrain as induced by severe plastic straining. The free MAUD software [32] was employed to refine the raw two-theta scans. Then, the dislocation density can be estimated by using the equation [33]:

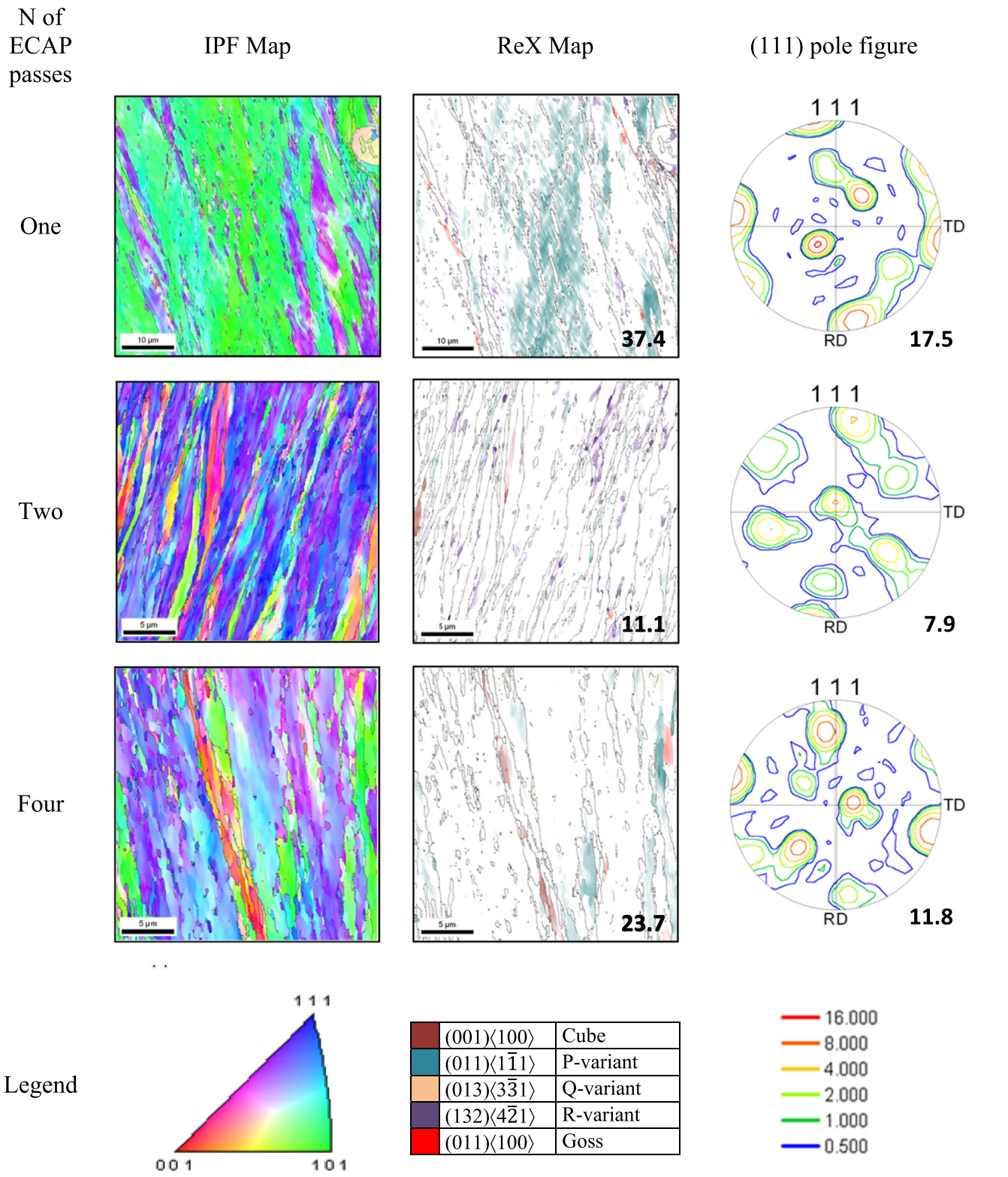

Fig. 4. IPF and recrystallization maps, (111) pole figures of the ST specimens subjected to ECAP. In "Legend" row there are standard stereographic triangle, texture components color bar and countour lines showing strength of texture. Right bottom values indicate in case of RX map (middle column) a fraction of recrystallized area and in (111) pole figures it shows the maximal level of a texture.

$$\rho = \frac{2\sqrt{3}\langle\varepsilon^2\rangle^{1/2}}{d \cdot b}, \tag{9}$$

where $\langle\varepsilon^2\rangle^{1/2}$ is a microstrain, d is crystallite size and b is Burgers' vector. Values of crystallite sizes and dislocation density are given in Tables 1 and 2 in the last columns and are summarized in Fig. 6.

Both values are smaller than those measured using TEM and EBSD. One can note that the dislocation density via X-ray is one order of magnitude smaller than that estimated by using the other methods.

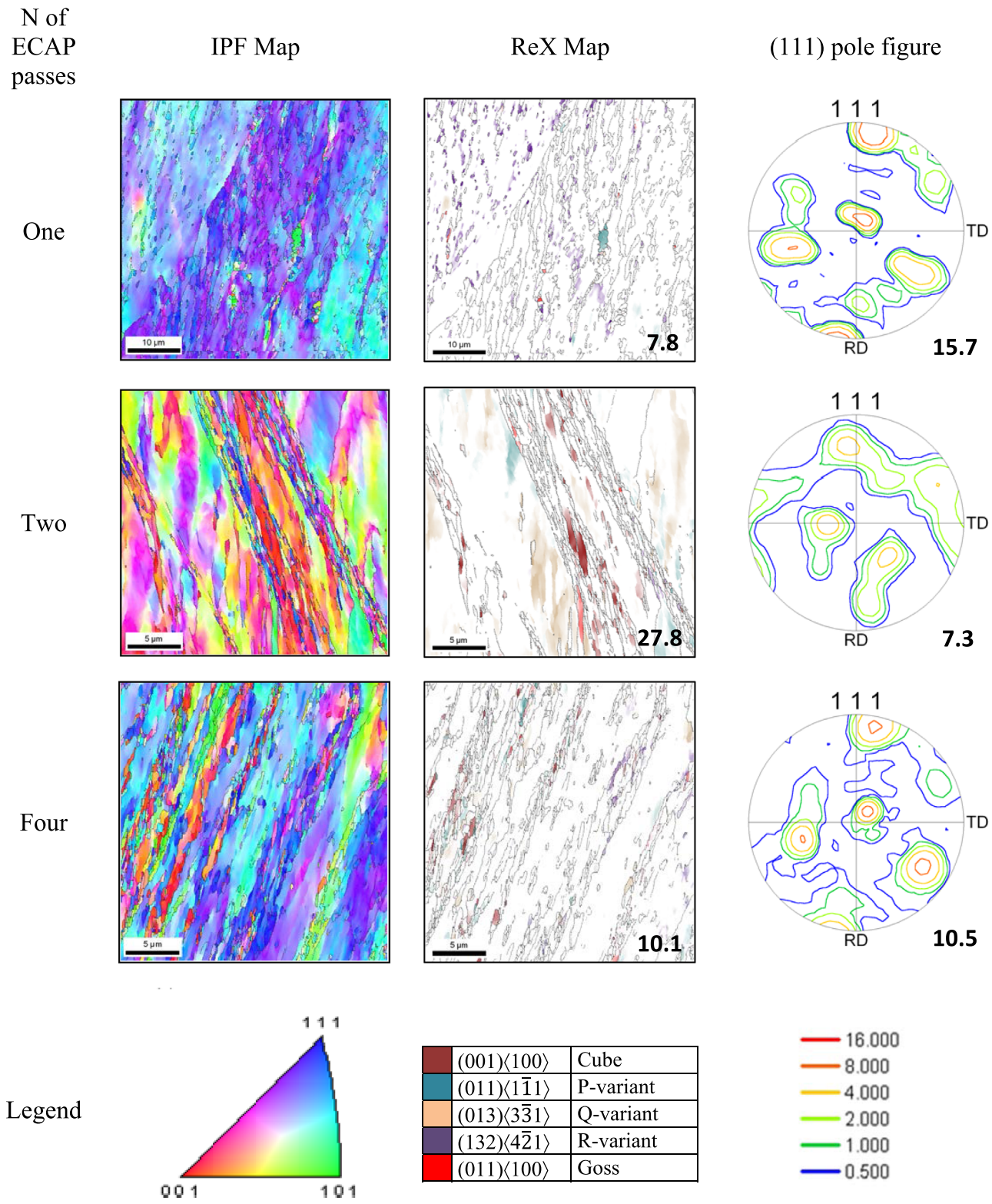

Fig. 5. IPF and recrystallization maps, (111) pole figures of the AT specimens subjected to ECAP. In "Legend" row there are standard stereographic triangle, texture components color bar and countour lines showing strength of texture. Right bottom values indicate in case of RX map (middle column) a fraction of recrystallized area and in (111) pole figures it shows the maximal level of a texture.

3.3. *Mechanical properties*

The engineering tensile stress–strain curves of the Cu–Cr–Zr alloy in both conditions and subjected to ECAP straining are shown in Fig. 7. The mechanical properties (YS, UTS and elongation to failure) are summarized in Fig. 8a and b. The shape of σ–ε curves is essentially the same in both conditions. The initial ST and AT samples are characterized by the pronounced strain hardening up to very high strains. The value of YS in the ST condition is slightly higher than that of a pure Cu [11,20], while aging provides an increase in YS by 160%. This is attributed to a small solid-solution hardening and a strong dispersion hardening in Cu–Cr alloys

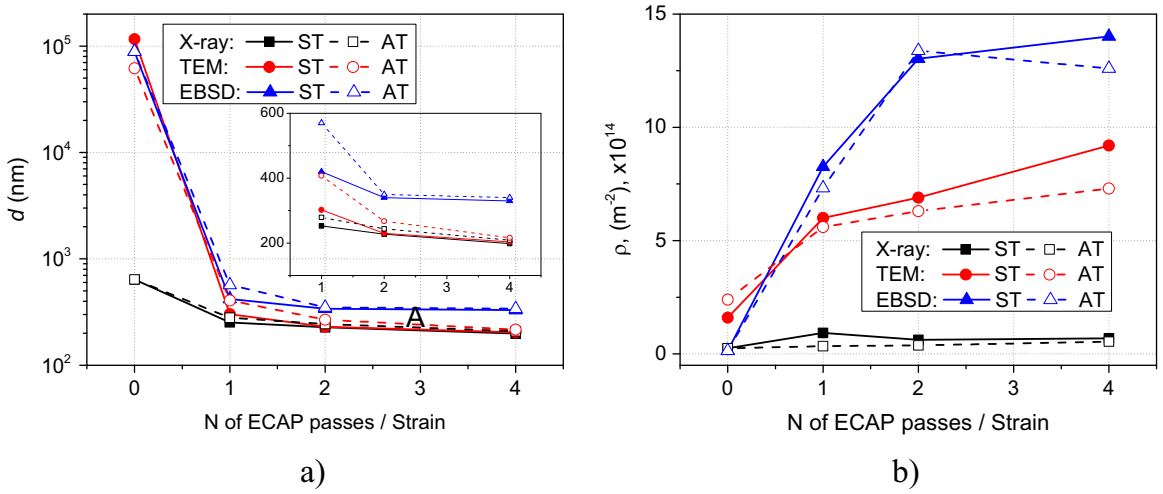

Fig. 6. Crystallite size (a) and dislocation density (b) as a function of accumulated strain or number of ECAP passes for solution treated and aged (b) conditions as a function of accumulated strain or number of ECAP passes evaluated by X-ray, TEM and EBSD. Insert in (a) depicts magnified view of crystallite size dependence in range from 1 to 5 passes of the ECAP.

[11,34]. An increase in the Cr content from 0.35 to 0.87% provides an increase in YS by 41% in the peak aged condition despite a decrease in the Zr content from 0.5 to 0.06% [11]. Therefore, the solid-solution hardening effects of Cr and Zr are relatively small and Cr is the main agent of dispersion hardening as suggested by several previous studies [7–12]. The large uniform and total elongations in the ST and AT samples are attributed to the stability of plastic flow. The ratio of UTS/YS is ~3.2 and ~2 for the ST and AT samples, respectively.

After ECAP the apparent steady state flow is attained after yielding at small strains. In the case of the ST condition (Fig. 8a), one can observe a gradual increase in strength with an increasing number of ECAP passes. This relates to the gradual increase of dislocation density as the deformation process progresses. Aged specimens show higher values of YS and UTS. Saturation in these values occurs immediately after one ECAP pass; YS and UTS do not differ significantly for AT specimens (Fig. 8b) after 2 and 4 ECAP passes. This may relate to the rapid increase in dislocation density due to precipitation strengthening. Surprisingly, the elongation to failure behaves non-monotonically and a noticeable increase in ductility is observed in the AT condition after 2 ECAP passes. This correlates with the increase of the fraction of the recrystallized area for the AT specimen recorded for the ECAP specimen after 2 passes (Fig. 5).

3.4. Electroconductivity

Measurements of electrical conductivity have revealed a typical behavior for deformed materials (Fig. 9): decreasing with increasing strain. However, there are two noticeable peculiarities. For the ST specimens, the electroconductivity decreases after the first ECAP pass and then slightly increases as straining progresses. For the AT condition, the electroconductivity decreases after one pass and saturates at this level during the following straining.

4. Discussion

In this report, there is a unique opportunity to compare the microstructural parameters obtained by using three different methods (TEM, EBSD and X-ray). In contrast to a Cu–0.86%Cr–0.1Zr alloy [11] the present material exhibited lamellar type microstructure after ECAP. It has been shown that the dislocation strengthening exceeds the grain size strengthening in the Cu–Cr–Zr alloy for all types of deformation structures [11]. This feature of the strengthening mechanism in the Cu–Cr–Zr alloy enables high strength and satisfactory electrical conductivity owing to the formation of deformation bands after small number of ECAP passes. Let us consider the relationship between the deformation

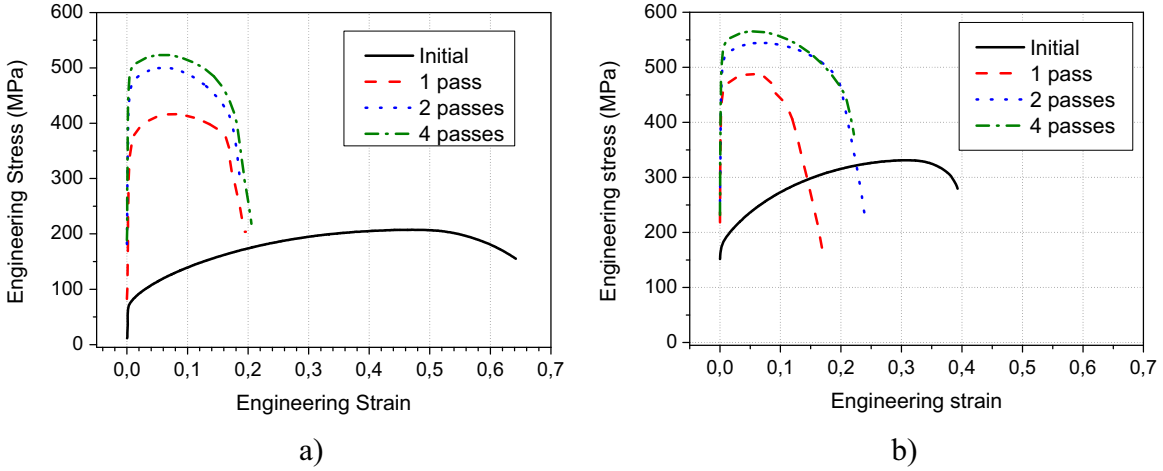

Fig. 7. Engineering stress–strain plot as a function of the number of the ECAP passes for solution treated (a) and aged (b) conditions of the CuCrZr alloy.

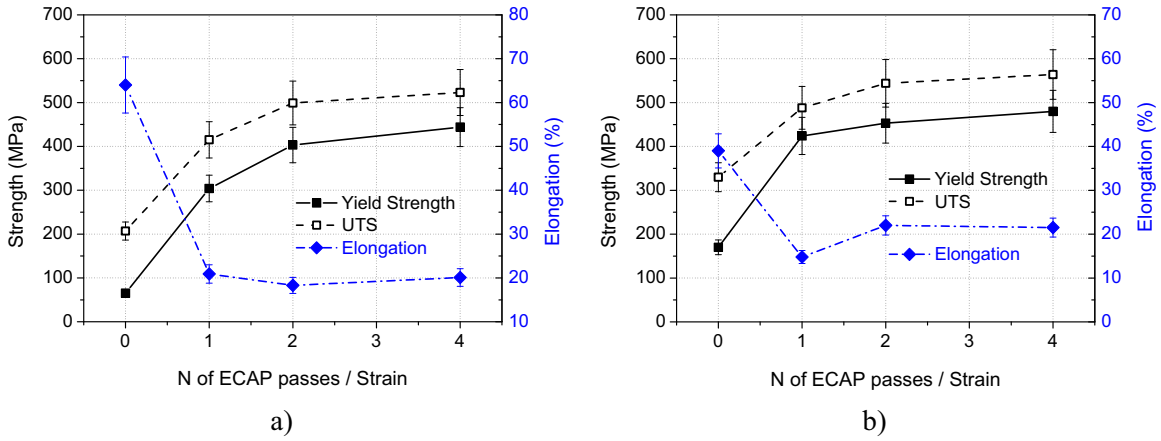

Fig. 8. Yield strength/UTS and elongation of the CuCrZr alloy in solution treated (a) and aged (b) conditions as a function of accumulated strain or number of ECAP passes.

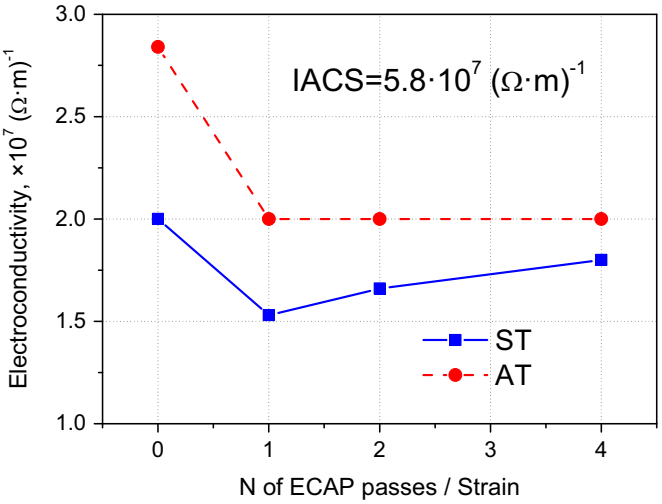

Fig. 9. Electroconductivity of CuCrZr alloy in solution treated and aged condition as a function of accumulated strain or number of ECAP passes.

structure and YS in the present Cu–0.3%Cr–0.5%Zr alloy.

In general, under the assumption that all mechanisms of strengthening contribute to the total increase in strength independently (which is not correct in many cases), a rule of additiveness can be applied: Total strength is a sum of lattice friction (or Peierls–Nabarro stress), solution strengthening, dispersion hardening, dislocation strengthening and grain size hardening (H–P). Assuming that the correct model is based on using copper as a matrix metal, one can estimate the contribution of different mechanisms:

- Friction lattice or Peierls–Nabarro stress for copper is 25 MPa.
- Solid solution strengthening is expressed as $\sigma_{SS} = K \cdot C$, where K is a constant and C is the concentration of alloying elements in the matrix (%wt). It is a linearized form of more complex relationship $\sigma_{SS} = Gb\epsilon^{3/2} \cdot C^{1/2}$, where $G=42.1$ GPa and $b=0.256$ nm are shear modulus and the magnitude of the Burgers vector of pure copper, correspondingly; $\epsilon = [\epsilon_a - \beta\epsilon_G]$ is a misfit strain due to a lattice distortion near solute atom.
- Dispersion hardening can be evaluated using the BKS model: assuming that the size of precipitates and their distribution do not change substantially during ECAP processing, contributions for the ST and AT conditions were estimated to be ~30 MPa for ST specimens and 147 MPa for AT specimens. It can be noted that for ST specimens, the large particles giving an increase of 30 MPa are probably not Cr-rich precipitates and will thus be left out of our analysis.
- Dislocation strengthening is defined as $\sigma_{DISL} \sim \alpha M G \sqrt{\rho}$, where α is the geometrical factor, $M \approx 3$ is the Taylor factor for fcc metals (it can be estimated from EBSD data), G is shear strength of pure copper and ρ is dislocation density.
- Grain size or Hall–Petch hardening $\sigma_{HP} = \sigma_0 + k/\sqrt{d}$, where $k=110$ MPa/μm$^{1/2}$. Note that the H–P relation was developed for materials of which the grain size was measured by using the intercept method using optical micrographs. For modern TEM and EBSD methods, intercept methods can be applied, but for X-ray, only the size of coherent domains can be evaluated, i.e., by using the Rietveld method.

Let us note that in general, all the above mentioned mechanisms are different ways to retard dislocation moving through grains, which can be active in all stages of deformation, and certain mechanisms may be activated with the progression of deformation, e.g., dislocation subboundaries may act as conventional grain boundaries in terms of their strength contribution as their misorientation increases during deformation [11]. In the present study, we took into account all boundaries with misorientation $\geq 5°$ for calculation of grain size strengthening because almost all deformation bands are bounded by such boundaries after $\varepsilon \sim 2$ and these boundaries are impenetrable obstacles to gliding dislocations [11]. Therefore, the structural strengthening that attributed to deformation bands could be evaluated after the second pass of ECAP since majority of deformation-induced boundaries have misorientation $< 5°$ after the first pass in both ST and AT samples [11]. In the next sections, the contribution of individual strengthening mechanisms to total strength will be calculated using the microstructural parameters measured by using TEM, EBSD and X-ray (taken from Tables 1 and 2).

4.1. Dislocation strengthening (TEM vs. EBSD vs. X-ray)

The values of dislocation density measured using TEM and EBSD (Table 2) are of the same order of magnitude and differ by approximately 1.5–2 times depending on the number of ECAP passes or accumulated strain. The highest value of dislocation density was detected for EBSD (except for the initial condition, where the highest dislocation density was measured for TEM). The lowest value of dislocation density was estimated from the X-ray experimental data. The difference in measured dislocation density for TEM and EBSD may be attributed to the fact that some dislocations might not be in diffraction conditions ($\mathbf{gb} \neq 0$) and that they do not appear in the bright field image. Fig. 10 represents the contribution (dashed lines) of dislocations to total strengthening.

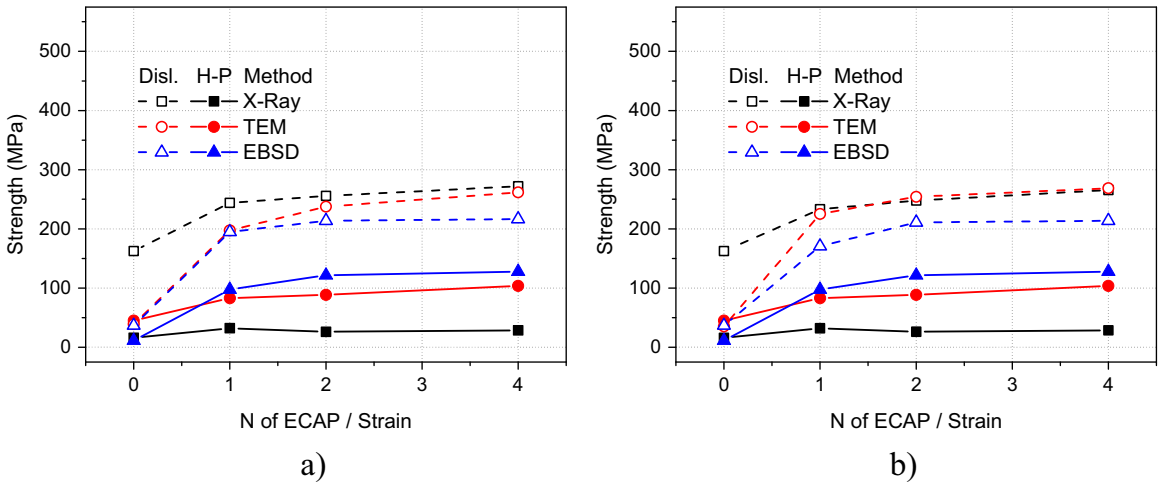

Fig. 10. Dislocation and Hall–Petch strengthening of CuCrZr alloy in solution treated (a) and aged (b) conditions as a function of accumulated strain or number of ECAP passes evaluated by X-ray, TEM and EBSD.

In general, there is no large difference in dislocation strengthening between ST and AT specimens.

4.2. Hall–Petch strengthening (TEM vs. EBSD vs. X-ray)

The grain size and thickness of deformation bands measured using the different methods are arranged in a direction similar to the dislocation density: the smallest size of coherent domains occurs for the X-ray, while the biggest grain size is detected using EBSD. In the case of the deformation bands (Figs. 3–5), the effective grain size was calculated as twice the distance between planar boundaries [35]. This leads to a unique situation where strengthening from dislocation and grain size measured using the different methods lead to more or less similar results, at least in the range of 100 MPa. This may explain why different reports show similar estimation of strengthening even when different experimental methods for evaluating microstructural parameters were used. Hall–Petch hardening (solid lines in Fig. 10), estimated via the different methods (TEM, EBSD and X-Ray), is similar for the ST and AT samples.

Fig. 11 represents the total strengthening estimated via the different methods and experimental data for the solution treated and aged specimens as functions of ECAP passes (or accumulated strain). It is apparent that the TEM and EBSD methods give strength closest to the experimental values. However, there is still a gap between the experimental and estimated values for ST specimens. Strengthening of the AT specimen estimated by the BKS model is in excellent agreement (Fig. 11b). The AT specimens demonstrate a higher strain hardening exponent than the ST samples. Therefore, deformation bands bounded by boundaries with moderate misorientations give a major contribution to grain size strengthening, since portion of HAB is small after four ECAP passes in both material conditions (Fig. 12). Meanwhile, for the AT specimens, portion of high angle boundaries starts to increase after 2 passes.

4.3. Models for precipitate hardening (Orowan model (BKS modification) vs. coherent model and elastic module change

In a recent report [11] on a Cu–0.86%Cr–0.1%Zr alloy subjected to ECAP in the solution treated condition, it was claimed that the modified Orowan model gives too high values for precipitation hardening for the Cr-rich particles distribution recorded in the experiment. The authors of [11] applied shearing mechanism, in which coherency strengthening and modulus strengthening operated [36–39]. This mechanism was used to explain the strain hardening observed in the Cu–0.86%Cr–0.1%Zr subjected to ECAP deformation [11], but they have some drawbacks: (i) for coherency strengthening, misfit strain is a poorly defined parameter and may change as Cr-particles grow; (ii) there is some uncertainty when

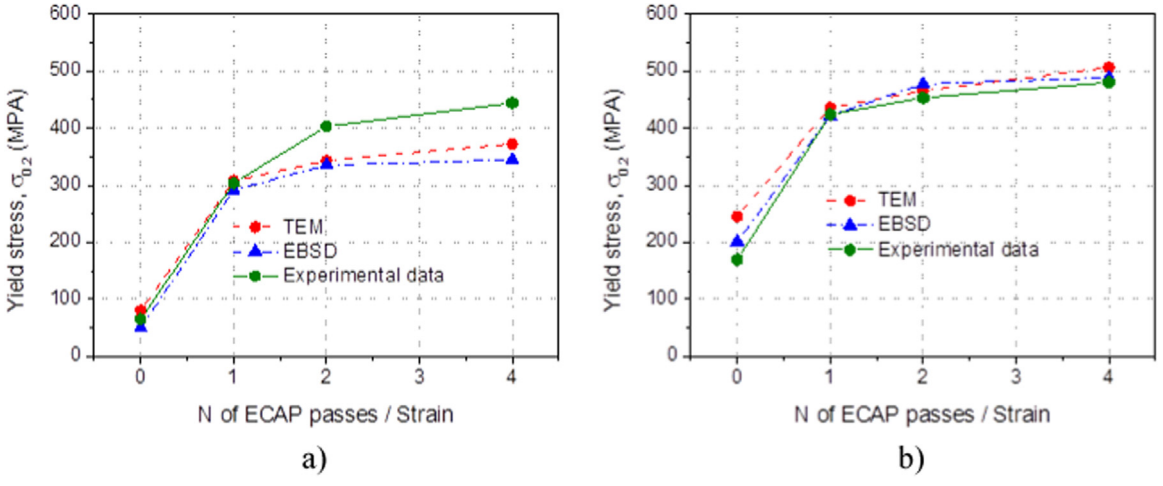

Fig. 11. Total strengthening and experimental YS of CuCrZr alloy in solution treated (a) and aged (b) conditions as a function of accumulated strain or number of ECAP passes evaluated by TEM and EBSD.

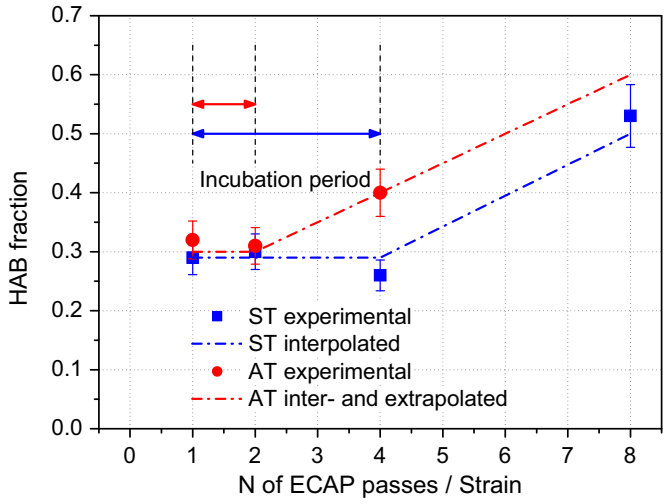

Fig. 12. Fraction of high-angle boundaries in the CuCrZr alloy in solution treated and aged condition as a function of accumulated strain or number of ECAP passes.

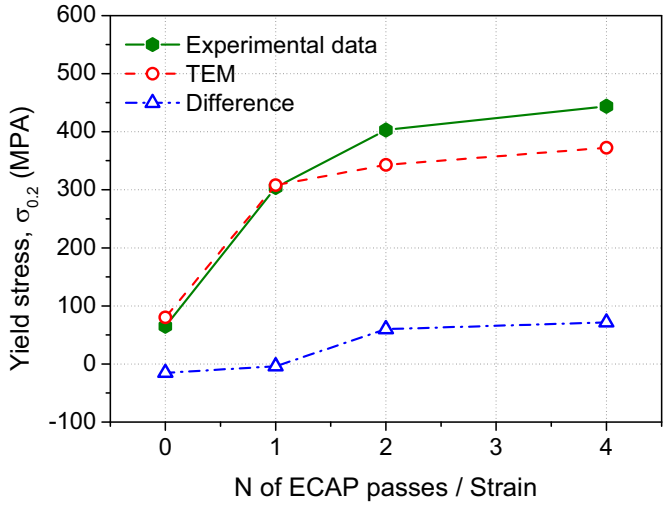

Fig. 13. Discrepancy between dislocation + Hall–Petch hardening (using TEM data) and experimental data for solution treated alloy as a function of accumulated strain or number of ECAP passes.

using the lattice parameter of chromium in a model related to change in the shear modulus because particles are not purely chromium. Instead, application of BKS modification of the Orowan model gives excellent agreement for the AT specimens (Fig. 11b) and still gives similar strengthening values for the ST samples (Fig. 11a). The maximal discrepancy between the calculated and experimental data is approximately 75 MPa for the ST specimen subjected to four ECAP passes. A possible explanation for the inconsistency between the model and experimental data can be deduced from the precipitation of Cr-rich particles during preheating prior to ECAP and processing at an elevated temperature. One can evaluate the hardening due to precipitation. The dash-dot line (triangles) in Fig. 13 shows the difference between experimental YS and the sum of dislocation hardening and Hall–Petch strengthening. It evolves non-monotonically with accumulated strain (or the number of ECAP passes). The difference between experimental and calculated data is approximately zero before ECAP and then rises to a value of approximately 75 MPa for the ST sample processed for four passes. From the appearance of the curve, one can deduce that there are two stages of strengthening: (i) incubation period, and (ii) precipitation hardening, in which particles start to grow. The incubation period is in good

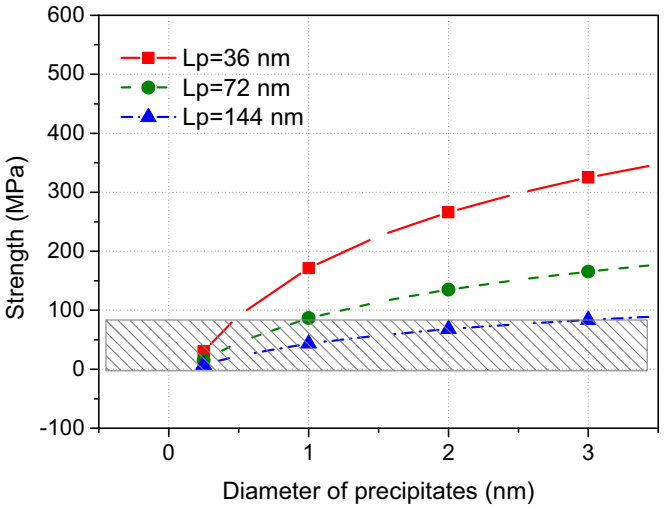

Fig. 14. Precipitation hardening by BKS model for different interparticles distance as a function of particles' size.

consistency with the time of delaying in accumulating high-angle boundaries (Fig. 12). Applying BKS model (Eq. (4)) one can plot the precipitation strengthening for different size of growing precipitates and for three different interparticle distances (36 nm, 72 nm and 144 nm) as a function of particle diameters (Fig. 14) in order to estimate the dynamic precipitation hardening during ECAP at an elevated temperature. It is rather unrealistic that the size of particles can be greater than 2.5 nm, which is the particle size of aged specimens. From Fig. 14, one can deduce that the interparticle distance is approximately 72 nm, which is similar to the one for AT samples, and that the precipitate size increases from 0.25 nm to 2 nm during preheating and ECAP processing of the solute treated specimens.

Therefore, Orowan bowing is the mechanism of dispersion strengthening in the present Cu–0.3%Cr–0.5%Zr alloy. It seems that increased Zr content led to Zr segregation at Cu/Cr interfaces that leads to the formation of Zr-enriched shell on Cr nanoscale dispersoids [40]. We may assume that this shell makes Cr dispersoids none-shearable and, therefore, the mechanism of interaction between gliding dislocations and nanoscale dispersoids changes from shearing to Orowan bowing.

4.4. Functional properties (Electroconductivity vs. strength and ductility)

Fig. 9 shows that both conditions (ST and AT) possess some saturation as the number of ECAP passes increases. Two remarks can be made before concluding: (i) ECAP processing does not harden the Cu–Cr–Zr alloy in both (ST and AT) conditions to the level for industrial usage ($\sigma_{0.2} > 650$ MPa), and (ii) decreasing electroconductivity supposes further thermomechanical treating of the ECAP specimens, which can lead to further precipitation hardening. However, both operations can be combined into one process of ECAP at higher (and supposedly optimal) temperature, as was recently suggested for Al-alloys [41] when both optimal parameters (strength and electrical conductivity) were achieved via optimization of the ECAP process (number of passes and processing temperature). From Fig. 14, one can deduce that precipitates shall grow to sizes larger than 4 nm.

5. Concluding remarks

New experimental observations and comprehensive analyses were performed to examine different known models for

strengthening mechanisms of Cu–0.3Cr–0.5Zr alloys subjected to ECAP processing via route Bc at a temperature of 400 °C in solution and aged treated conditions. Previous reports published used more complicated models involving coherency or/and modulus strengthening for explanation of hardening CuCrZr alloys. Such models include a number of parameters which are problematical to estimate correctly: i.e. a fraction of coherent precipitates or misfit strain. In contrary, we have found that Bacon–Kocks–Scattergood modification of Orowan model is sufficient for acceptable description of precipitation hardening of AT specimens during ECAP processing and it gives an excellent agreement with experimental data. Discrepancy between experiment and model for ST specimens disappears after taking into consideration additional precipitating of supersaturated solid solution during preheating and ECAP processing. A novel phenomenological model for dynamic strengthening during ECAP processing of the alloy in supersatured state was developed on the base of our experimental data and from Atomic Tomography Probe data published earlier. Additionally, we were able to compare the microstructural parameters for this alloy acquired by different experimental methods such as TEM, EBSD and X-ray.

Acknowledgments

The financial support received from the Ministry of Education and Science of the Russian Federation, Russia, under Grant no. 14.575.21.0005 (ID number RFMEFI57514X0005) is gratefully acknowledged. The authors are grateful to the personnel of the Joint Research Centre, Belgorod State University, for their assistance with instrumental analysis.

References

[1] A.I. Topuz, Mater. Sci. Eng. A 627 (2015) 381–390.
[2] J.B. Correia, H.A. Davies, C.M. Sellars, Acta Mater. 45 (1997) 177–190.
[3] ITER Joint Central Team, J. Nucl. Mater. 212–215 (1994) 3–10.
[4] Q. Liu, X. Zhang, Y. Ge, J. Wang, J.-Zh. Cui, Metall. Mater. Trans. A 37A (2006) 3233–3238.
[5] I.S. Batra, G.K. Dey, U.D. Kulkarni, S. Banerjee, J. Nucl. Mater. 299 (2001) 91–100.
[6] G. Ghosh, J. Miyake, M.E. Fine, JOM 49 (1997) 56–60.
[7] A. Belyakov, M. Murayama, Y. Sakai, K. Tsuzaki, M. Okubo, M. Eto, T. Kimura, J. Electron. Mater. 35 (2006) 2000–2008.
[8] K.X. Wei, W. Wei, F. Wang, Q.B. Dua, I.V. Alexandrov, J. Hu, Mater. Sci. Eng. A 528 (2011) 1478–1484.
[9] A. Vinogradov, V. Patlan, Y. Suzuki, K. Kitagawa, V.I. Kopylov, Acta Mater. 50 (2002) 1639–1651.
[10] I. Shakhova, Z. Yanushkevich, I. Fedorova, A. Belyakov, R. Kaibyshev, Mater. Sci. Eng. A 606 (2014) 380–389.
[11] R. Mishnev, I. Shakhova, A. Belyakov, R. Kaibyshev, Mater. Sci. Eng. A 629 (2015) 29–40.
[12] A. Chibihi, X. Sauvage, D. Blavette, Acta Mater. 60 (2012) 4575–4585.
[13] T. Fujii, H. Nakazawa, M. Kato, U. Dahnem, Acta Mater. 48 (2000) 1033–1045.
[14] J.-H. Su, Q.-M. Dong, P. Liu, H.-J. Li, B.-X. Kang, Mater. Sci. Eng. A 392 (2005) 422–426.
[15] H. Fuxiang, M. Jusheng, N. Honglong, G. Zhiting, L. Chao, G. Shumei, Y. Xuetao, W. Tao, L. Hong, L. Huafen, Scr. Mater. 48 (2003) 97–102.
[16] Y. Estrin, A. Vinogradov, Acta Mater. 61 (2013) 782–817.
[17] O.R. Valiakhmetov, R.M. Galeyev, G.A. Salishchev, Phys. Met. Metallogr. 10 (1990) 204–206.
[18] R.Z. Valiev, T.G. Langdon, Prog. Mater. Sci. 51 (2006) 881–981.
[19] G.V. Zel'dovich, N.Y. Frolova, I.V. Khomskaya, A.E. Kheifets, E.V. Shorokhov, P. A. Nasonov, Phys. Met. Metallogr. 115 (2014) 465–470.
[20] F.H. Dalla Torre, E.V. Pereloma, C.H.J. Davies, Acta Mater. 54 (2006) 1135–1146.
[21] A.P. Zhilyaev, T.G. Langdon, Prog. Mater. Sci. 53 (2008) 893–979.
[22] D.V. Shangina, J. Gubicza, E. Dodony, N.R. Bochvar, P.B. Straumal, N. Yu Tabachkova, S.V. Dobatkin, J. Mater. Sci. 49 (2014) 6674–6681.
[23] M.T. Perez-Prado, A.P. Zhilyaev, Phys. Rev. Lett. 102 (175504) (2009) 1–4.
[24] N. Takata, Y. Ohtake, K. Kita, K. Kitagawa, N. Tsuji, Scr. Mater. 60 (2009) 590–593.
[25] H.M. Rietveld, J. Appl. Crystallogr. 2 (1969) 65–71.
[26] ⟨http:// http://maud.radiographema.com/⟩.
[27] F.M. Smits, Bell Syst. Tech. J. 34 (1958) 711–718.
[28] F.J. Humphreys, M. Hatherly, Recrystallization and Related Annealing Phenomena, 2nd ed, Elsevier, Oxford, 2005.
[29] D.J. Bacon, U.F. Kocks, R.O. Scattergood, Philos. Mag. 28 (1973) 1241–1263.
[30] H.J. Frost, M.F. Ashby, Deformation-Mechanism Maps, The Plasticity and Creep of Metals and Ceramics, Pergamon, Oxford (UK), 1982.
[31] A.P. Zhilyaev, I. Shakhova, A. Belyakov, R. Kaibyshev, T.G. Langdon, Wear 305 (2013) 89–99.
[32] ⟨http://maud.radiographema.com/⟩ (MAUD free software).
[33] R.E. Smallman, K.H. Westmacott, Philos. Mag. 2 (1957) 669–683.
[34] A. Bachmaier, G.B. Rathmayr, M. Bartosik, D. Apel, Z. Zhang, R. Pippan, Acta Mater. 69 (2014) 301–313.
[35] X. Zhang, A. Godfrey, X. Huang, N. Hansen, Q. Liu, Acta Mater. 59 (2011) 3422–3430.
[36] E. Nembach, Phys. Status Solidi A 78 (1983) 571–581.
[37] R. Ahmadi, B. Sonderegger, E. Povoden-Karadeniz, A. Falahati, E. Kozeschnik, Mater. Sci. Eng. A 590 (2014) 262–266.
[38] I. Holzner, E. Kozeschnik, Mater. Sci. Eng. A 527 (2010) 3546–3551.
[39] M.R. Ahmadi, E. Povoden-Karadeniz, K.I. Oksuz, A. Falahati, E. Kozeschnik, Comput. Mater. Sci. 91 (2014) 173–186.
[40] M. Hatakeyama, T. Toyama, Y. Nagai, M. Hasekawa, M. Eldrup, B.N. Singh, Mater. Trans. 49 (2008) 518–521.
[41] M. Yu Murashkin, I. Sabirov, X. Sauvage, R.Z. Valiev, J. Mater. Sci. 51 (2016) 33–49.